Coordination Chemistry Reviews 254 (2010) 1383–1396

Contents lists available at ScienceDirect

Coordination Chemistry Reviews

journal homepage: www.elsevier.com/locate/ccr

Review

Quantum chemical interpretation of redox properties of ruthenium complexes with vinyl and TCNX type non-innocent ligands

Stanislav Záliš[a,*], Rainer F. Winter[b,*], Wolfgang Kaim[c]

[a] J. Heyrovský Institute of Physical Chemistry, v.v.i., Academy of Sciences of the Czech Republic, Dolejškova 3, CZ-18223 Prague, Czech Republic
[b] Institut für Anorganische Chemie der Universität Regensburg, D-93040 Regensburg, Germany
[c] Institut für Anorganische Chemie der Universität Stuttgart, D-70569 Stuttgart, Germany

Contents

ARTICLE INFO

Article history:
Received 9 November 2009
Accepted 15 February 2010
Available online 23 February 2010

Keywords:
Density functional theory
Non-innocent ligands
Redox properties
Ruthenium
Spectroelectrochemistry
Molecular properties

ABSTRACT

This review provides an overview of density functional theory (DFT) calculations in a consequence with spectroelectrochemical measurements on mononuclear and symmetrically or unsymmetrically bridged di- and tetranuclear ruthenium complexes of vinyl and TCNX ligands. The DFT approach is used for the calculations of molecular structures, vibrational frequencies, electronic and electron paramagnetic resonance (EPR) spectral data. DFT calculations enable us to identity the primary redox site and the electron and spin-density distribution between the individual components for the individual redox congeners. The DFT technique reproduces the spectral properties of the presented complexes and their radical ions. The generally close correspondence between experimental and quantum chemical results demonstrate that modern DFT is a powerful tool to address issues like ligand non-innocence and electron and spin delocalization in systems containing both redox-active metal ions and redox-active ligands.

1. Introduction

During redox changes within metal complexes containing one or several non-innocent redox-active ligands the electron can be accepted by or released from either a metal center or any of these ligands. The electron density redistribution in the course of the electron transfer will affect the variation of physical properties and

* Corresponding authors.
E-mail addresses: zalis@jh-inst.cas.cz (S. Záliš), rainer.winter@chemie.uni-regensburg.de (R.F. Winter).

0010-8545/$ – see front matter © 2010 Elsevier B.V. All rights reserved.
doi:10.1016/j.ccr.2010.02.020

allow for the possible formation of valence tautomers, which can be distinguished by their absorption properties in the visible and the near infrared (NIR). Knowledge of the character of redox orbitals is thus generally required in order to interpret physical properties and their variation due to redox changes [1]. Quantum chemical calculations can help to understand and adequately interpret the mechanism and consequences of electron transfer processes. Therefore, quantum chemical calculations of electronic structure are frequently used for the interpretation of experimental properties and to probe the extent of electron delocalization between individual redox centers in more complex systems featuring more than just one redox-active subunit. Any meaningful discussion requires to examine carefully all possible valence tautomers and to look for the lowest energy configuration. At present, the DFT method is preferably used for computational studies of large systems and their properties [2–9]. This contribution will illustrate the use of DFT in electronic structure calculations on ruthenium complexes containing different types of non-innocent ligands.

The chemistry of vinyl ruthenium complexes has been widely explored since the late 1970s. Reviews of their synthesis from corresponding hydride precursors and terminal alkynes, the mechanism of the so-called "hydroruthenation" process [10,11], their further modification through substitution of one or more phosphine ligands or the chloride ligand, and the ready interconversion between penta- and hexacoordinated derivatives $RuCl(CH{=}CHR)(CO)(PR_3)_2$ and $RuCl(CH{=}CHR)(CO)(PR'_3)_2(L)$ (L = neutral monodentate ligand such as phosphine, pyridine, isonitrile, CO and the like) have appeared in the literature [12]. Compared to the wealth of preparative and spectroscopic studies on vinyl ruthenium complexes, their electrochemical properties were largely unexplored before we entered this field. The notable exception is Caulton's and Tilset's study on the oxidatively induced reductive coupling of vinyl and alkynyl ligands in $Ru(CH{=}CHPh)(C{\equiv}CPh)(CO)(P^tBu_2Me)_2$ to give the corresponding 1,4-diphenylbut-3-ene-1-yne [13]. While this experimental result already suggests a significant ligand contribution to the oxidation process, it was only recently that the amount of that contribution and, thus, the strongly non-innocent character of the vinyl ligand in that particular environment came to light. Therefore we initiated a combination of experimental and quantum chemical studies in order to provide detailed insight into the electronic structure of such vinyl ruthenium complexes as is summarized below.

Mono- and dinuclear ruthenium complexes $RuCl(CH{=}CHR')(CO)(PR_3)_2$ and $RuCl(CO)(PR_3)_2(CH{=}CH{-}X{-}CH{=}CH)RuCl(CO)(PR_3)_2$ containing substituted vinyl ligands form the first group of complexes presented. DFT calculations on neutral diruthenium complexes with substituted vinyl ligands indicate a mixed π-ligand/metal character of the highest lying molecular orbital (HOMO). Upon the first and second oxidations, electrons are stepwise withdrawn from the HOMO. Calculated spin densities of the radical cations thus correspond closely to HOMO orbital coefficients. The calculations confirm experimental results of ligand dominated oxidation processes and smaller contributions from the metal atoms. Upon oxidation of the dinuclear divinyl-bridged complexes the CO-band shifts to higher frequency and slightly splits. DFT calculations reproduce the experimentally observed variations of CO stretching frequencies. UV–vis spectra and their variations during stepwise oxidation are also reproduced by TD-DFT calculations. Here, the electron density can be reorganized in different ways in the course of excitation.

A shorter chapter on tetraruthenium complexes of the non-innocent oxidizable ligand tetrakis(4-styryl)ethene (TSTE) or of reducible ligands of the TCNX type such as tetracyanoethene (TCNE) and 7,7,8,8-tetracyano-*p*-quinodimethane (TCNQ) [14] concludes this review. Metal complexes of the TCNX ligands [15,16] are of special interest because of low-dimensional electrical conductivity and unusual magnetic properties, including ferri- and ferromagnetism at relatively high temperatures, with potential applications in spintronics and molecular magnetism [17–19]. DFT calculations of these systems can clarify the electron density redistribution in TCNX bridged systems and help to understand the intriguing experimental results.

The presence of several redox-active components allows for several possible redox pathways which are reflected in different spectral properties. Quantum chemical calculations enable us to assign the proper oxidation state distribution of individual ligands and the metal atoms and to interpret IR and UV–vis spectra and other physical properties along the various redox series.

2. Theoretical and experimental approaches

2.1. Density functional theory

The transition metal complexes presented in this study are large and the only practical method for their electronic structure calculations is DFT. Several review articles describing the application of DFT in the field of transition metal complexes have been published recently [2,3,9]. Therefore only specific details with regard to the interpretation of redox and spectral properties are provided in this section.

We present results obtained by using the Gaussian 03 [20] and ADF [21] program packages. Within G03 calculations the quasirelativistic effective core pseudopotentials and the corresponding optimized set of basis functions for Ru [22,23] and 6–31G* [24,25] polarized double-ζ Gaussian basis sets or Dunning's correlation consistent basis sets cc-pvdz [26–28] for the remaining atoms were employed. Within ADF Slater type orbital (STO) basis sets of triple-ζ quality with polarization functions were employed with the exception of the CH_3 substituents on P atoms which were described on a double-ζ basis. The inner shells were represented by a frozen core approximation, *viz.* 1s for C, N, 1s–2p for P, Cl and 1s–3d for Ru were kept frozen. Several pure and hybrid density functionals were used: pure exchange correlation BP86 [29,30] and BPW91 [29,31], hybrid B3LYP [32] and PBE0 [33,34], and meta-GGA M05-2x [35,36].

The geometry optimizations were followed by frequency calculations in order to characterize the stationary state obtained and to interpret IR spectra. Open-shell systems were calculated by the spin unrestricted KS approach (UKS). Due to the cancellation of errors the harmonic frequencies obtained by pure density functionals like BP86 and BPW91 predict ground state IR spectra reasonably well [37,38]. Hybrid density functionals are often needed for a better description of the properties and electron density distribution of radical ions. Harmonic frequencies calculated by hybrid functionals require scaling in order to get quantitative agreement with experimental IR frequencies [39]. Electron densities and unpaired spins in open-shell systems can be distributed in different ways, being either delocalized over the whole system or localized on one part of the molecule. Such valence tautomers are usually close in energy and difficult to obtain by standard approaches. The symmetry broken approach [3,40–43] was used for finding the individual states corresponding to different electron density localization. The wavefunctions of optimized structures were checked for stability [44]. Only solutions corresponding to stable wavefunctions are presented throughout this work.

Electronic transitions were calculated by the time-dependent DFT (TD-DFT) method [45]. Solvent effects within TD-DFT were described by the polarizable continuum model (PCM) [46,47]. It was shown that TD-DFT applied for open-shell systems gives in some cases good agreement with experimental spectra but fails in other cases [48], therefore caution is warranted when the interpreting the electronic spectra of radical ions. EPR parameters

were calculated by the ADF program [49,50]. The scalar relativistic (SR) effects were described by zero order regular approximation (ZORA)[51]. The *g*-tensor was obtained from a spin-nonpolarized wave function after incorporating the spin-orbit (SO) coupling by first-order perturbation theory from ZORA Hamiltonian in the presence of a time-independent magnetic field [52,53]. Solvent effects within ADF were described a conductor-like screening model (COSMO)[54,55]. IR and UV–vis spectra were modeled by the GaussView software; spectral features were approximated as Lorentzian curves.

2.2. Spectroelectrochemical techniques

In order to generate and spectroscopically characterize the oxidized forms of vinyl ruthenium complexes, which sometimes are chemically rather reactive, we mostly resorted to spectroelectrochemical techniques. Here, the species of interest is generated by controlled potential electrolysis inside an optically transparent thin-layer electrolysis cell with continuous spectroscopic monitoring of the electrolysis progress. Our cell is home-built but closely follows the design of Hartl et al. [56]. Its construction from CaF_2 windows makes it amenable to spectroscopic studies over the entire UV–vis–NIR–mid-IR range down to ca. 1000 cm^{-1}. The designs of such experiments and their limitations and possible pitfalls have already been commented on and the interested reader is directed to relevant literature [57–60]. For practical purposes (in particular its higher boiling point) these experiment were performed in 1,2-$C_2H_4Cl_2$/NBu_4PF_6 rather than in the CH_2Cl_2/NBu_4PF_6 electrolyte system used otherwise for the recording of electroanalytical data. EPR work is based on the electrolysis of the compound under investigation inside the EPR tube with a simple two-electrode arrangement. Experimental details to these procedures can be found in our original papers that are cited in *References*.

3. Redox and spectral properties of ruthenium complexes with substituted vinyl ligands

3.1. Mononuclear Ru complexes

The metal *versus* vinyl ligand contribution to the frontier orbitals (FMOs) depends on the mutual positions of the appropriate metal d levels and the π orbitals of the vinyl ligand and their variations. Effects of such variation are nicely demonstrated by systems which allow us to study how (i) extending the π-system of the vinyl ligand, (ii) varying the *para*-substituent in styryl complexes (iii) manipulating the electron density at the metal atom, and (iv) varying the degree of coordinative saturation at the metal atom affect the bonding, the redox properties and metal *versus* ligand contribution to the redox orbitals. Combined theoretical and experimental studies of mononuclear ruthenium complexes monitor the electronic structure response on any of these variations, thus setting the ground for an understanding of more complex systems comprising two or more such moieties.

3.1.1. Tuning non-innocence by extension of the ligands' π-system

The extension of the π-system of vinyl ligands brings the ligand π-orbitals closer to Ru d levels, increases the π-conjugation within the entire system and thus strongly influences its redox properties. This effect was studied on penta- and hexacoordinated vinyl ruthenium complexes RuCl(CH=CHR)(CO)$(PR'_3)_2$ and RuCl(CH=CHR)(CO)$(PR'_3)_2$(py) with R = ^{n}butyl, phenyl or 2-pyrenyl and R′ = ^{i}Pr or Ph (see Chart 1). These complexes were prepared, characterized spectroscopically and, in part, by X-ray crystallography [61].

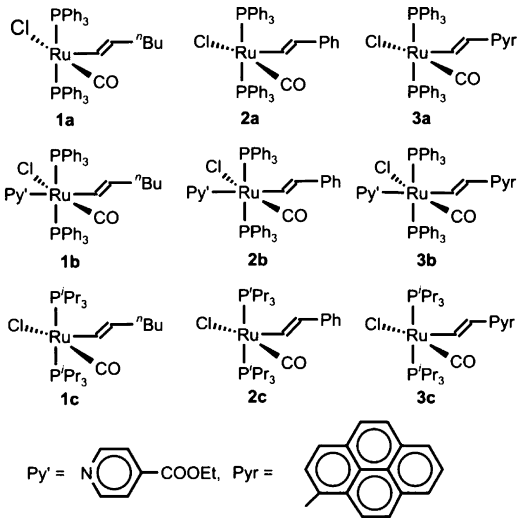

Chart 1. The vinyl complexes employed in this study.

In order to keep computational time at a reasonable limit, the phosphine ligands were modeled as PMe_3. The effect of such simplification was probed by calculations on the model complexes RuCl(CH=CHMe)(CO)$(PR'_3)_2$ with R′ = Me, ^{i}Pr or Ph. DFT-calculated structures and properties were compared to fully optimized **1c**. Optimized structures of the model and real complexes generally agree well [61,62]. In addition, the character of the frontier orbital of the model RuCl(CH=CHMe)(CO)$(PMe_3)_2$ (**1c^{Me}**) and of the fully optimized real complex **1c** differs only marginally. The experimentally observed blue shifts of the $\tilde{\nu}$(CO) band due to replacement of ^{i}Pr by Ph and upon oxidation are well described. These results indicate that substitution of the P^iPr_3 or PPh_3 ligands of the real complexes by PMe_3 does not overly compromise the accuracy of our calculations and can be used for DFT study of vinyl ruthenium complexes. These PMe_3 substituted model complexes are hereafter indicated by the "Me" superscript.

Fig. 1 shows the shapes of frontier orbitals for model complexes **1c^{Me}**, **2c^{Me}**, and **3c^{Me}**. For models of the hexacoordinated systems **1b^{Me}**, **2b^{Me}**, and **3b^{Me}** similar trends in the FMO composition were obtained. The major difference between the penta- and hexacoordinated systems pertains to the nature of the LUMO, which changes from a RuCl(CO)$(PR_3)_2$ based one to essentially a π* orbital of the pyridine ligand. For the propenyl and hexenyl systems **1c^{Me}** and **1c** the HOMO is fully delocalized over the Ru-vinyl entity. Vinyl ligand contributions to the HOMO become even more important when π-substituents are added and increase when going from **1c^{Me}** to **3c^{Me}**. Oxidation leads to an electron withdrawal from the respective HOMOs. Calculated spin densities for their corresponding oxidized forms as they are depicted in Fig. 2 confirm the trend deduced from the HOMO compositions.

The oxidation-induced shift of $\tilde{\nu}$(CO) provides an ideal tool for gauging the metal contribution to the oxidation process. Removal of a full unit charge from a metal atom is expected to increase the energy of the CO stretch by 100–150 cm^{-1} as less electron density is transferred from the metal atom to the π* orbitals of the carbonyl ligand [63]. Spectroelectrochemical measurements [61] indicate substantially lower shifts of $\tilde{\nu}$(CO) than is expected in the case of a metal centered redox process. Geometry optimisations followed by vibrational analysis performed for the neutral forms and the oxidized mono- and dications of the model complexes have shown that the experimental variation of IR parameters $\tilde{\nu}$(CO) and $\tilde{\nu}$(C=C) due to successive oxidations is well described by the calculated CO and C=C stretching frequencies.

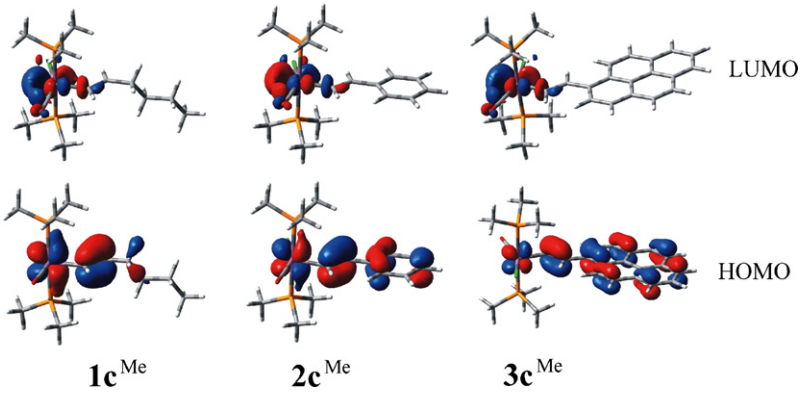

Fig. 1. Contour plots of the frontier orbitals of complexes **1c**^{Me}, **2c**^{Me}, and **3c**^{Me}.

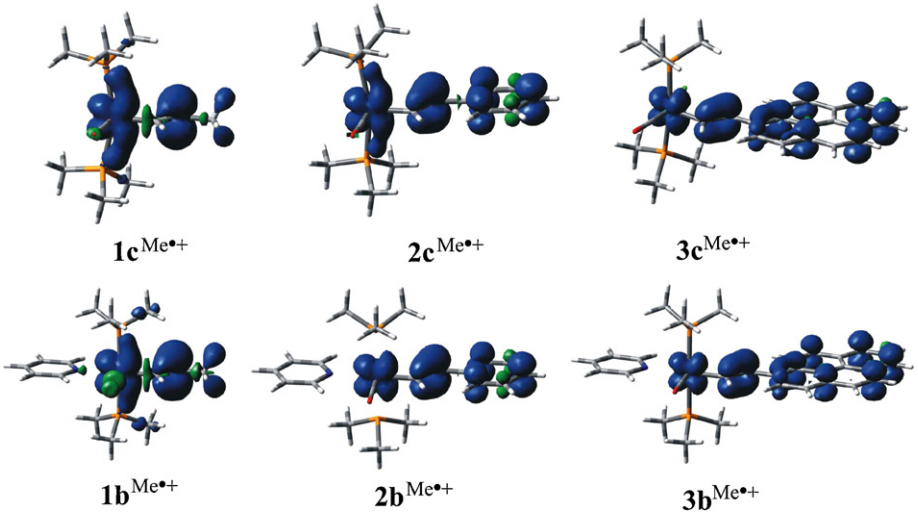

Fig. 2. Contour plots of spin densities for complexes **1c**$^{Me\bullet+}$, **2c**$^{Me\bullet+}$, **3c**$^{Me\bullet+}$, **1b**$^{Me\bullet+}$, **2b**$^{Me\bullet+}$, and **3b**$^{Me\bullet+}$.

In agreement with experimental results calculated stretching CO frequencies show the expected decrease of oxidation-induced CO-band shifts with decreasing HOMO metal character. Taking the redox pairs $Ru(PR_3)_2(CO)_3^{0/+}$ as benchmark systems and assuming a CO-band shift of 130 cm^{-1} for a ruthenium centered process, the metal contribution to oxidation of the P^iPr_3 complexes can be estimated as ca. 60% (**1c**), 50% (**2c**) and as ca. 35% (**3c**) of that in the benchmark systems. These data are in agreement with calculated HOMO compositions and indicate that metal contribution to the occupied frontier levels decreases as the π-conjugation of the vinyl ligand increases. This clearly justifies denoting the vinyl ligands in that particular environment as "non-innocent".

Recent examples of Ru(III) alkynyl complexes document close correlations between (calculated) metal contributions to the SOMO and the Δ*g* parameter [64–67]. EPR spectra of genuine Ru(III) paramagnetic species generally display axial or rhombic *g*-tensors with large *g*-anisotropies, *i.e.* large differences between the individual components of the *g*-tensor, and average *g*-values distinctly different from the free electron value g_e of 2.0023 [66–70]. Organic radicals, on the other hand, routinely display richly structured isotropic signals at room temperature, *g*-values close to that of the free electron and too small *g*-value anisotropies to be resolved in the X-band. EPR spectroscopy is thus ideally suited to probe for the character of the vinyl complexes' radical cations. The experimentally observed deviations of the average *g*-values from g_e and *g*-anisotropies Δ*g* are generally small and systematically decrease with increasing π conjugation. This confirms the above conclusions of an increasing ligand contribution to the SOMO orbitals as the covalency of the Ru-vinyl bond increases and more spin density is shifted onto the ligand. Calculated EPR parameters fully reproduce the experimental data [61].

3.1.2. *Effect of the para-substituent in styryl complexes on ligand non-innocence*

Another possibility of how to influence the position of the ligand π-orbitals in ruthenium styryl complexes is the replacement of the *para*-hydrogen atom on the phenyl ring in $RuCl(CH{=}CHPh)(CO)(PR'_3)_2$ by different substituents (Chart 2) [71]. Complexes with differently substituted styryl ligands having donor or acceptor substituents in the *para*-position were prepared and characterized by spectroscopic, electrochemical and spectroelectrochemical methods. Quantum chemical studies (G03/PBE0) of the substituent effect within these complexes were carried out for the series of model complexes $RuCl(CH{=}CHC_6H_4\text{-}4\text{-}X)(CO)(PMe_3)_2$

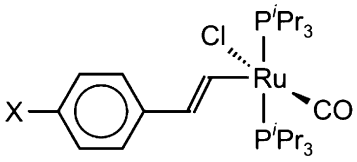

X = NMe_2, OMe, F, H, COOMe, CN, CF_3, NO_2

Chart 2. *para*-Substituted ruthenium styryl complexes $RuCl(CH{=}CHC_6H_4\text{-}4\text{-}X)(CO)(P^iPr_3)_2$.

(X = NMe_2, OMe, F, COOMe, CN, CF_3, NO_2) with the phosphine ligands modeled as PMe_3. The variation of the substituent strongly influences the character of the frontier orbitals and, consequently, the redox properties. Thus, the measured first oxidation potentials are highly sensitive to the nature of X and vary from −0.19 V for X = NMe_2 to +0.47 V for X = NO_2 when referenced to the Fc/Fc^+ scale. The electronic effect of the *para*-substituent is also reflected by the variation of the CO stretching energies in the neutral and the oxidized forms of these complexes and the relative magnitudes of the oxidation-induced CO-band shift by the modification of X. Quantum chemical results correlate with experimental variation of ν(CO) (see Fig. 3). Systematic effects of the *para*-substituent are also seen on a variety of other properties such as the ^{13}C and ^{1}H NMR shifts of the carbon atoms and the protons of the vinyl substituent, the spectral position of the low-energy bands in the electronic spectra of the radical cations and on the isotropic (or average) *g*-values and the *g*-anisotropies. Experimental and calculated EPR parameters agree well and show that the average *g*-values and *g*-anisotropies both increase as X becomes a stronger electron acceptor, which increases the metal contribution to the HOMO of the neutral complexes and to the SOMO of their corresponding radical cations. These were traced by the experimental EPR data and confirmed by calculated *g*-values.

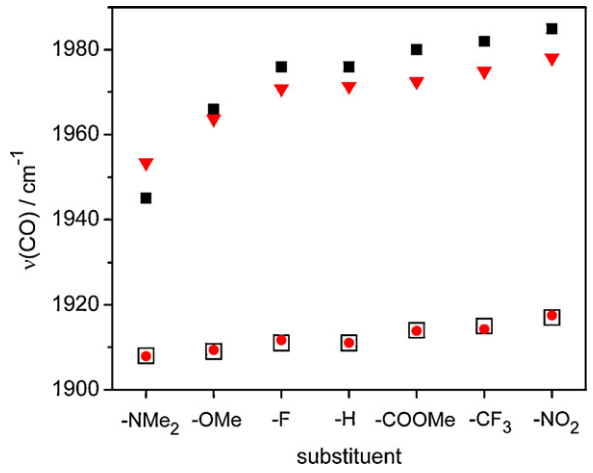

Fig. 3. Comparison of experimental ν(CO) IR frequencies of RuCl(CH=CHC_6H_4-4-X)(CO)$(PR_3)_2$ (exp.: R = ^{i}Pr, calc. R = Me) in the neutral (black empty squares) and the mono-oxidized states (black full squares) with DFT (G03/PBE0) calculated ones (red circles and triangles for the neutral and the mono-oxidized states, respectively). DFT-calculated values for model complexes RuCl(CH=CHC_6H_4-4-X)(CO)$(PMe_3)_2$ were scaled by a factor of 0.9365.

3.2. Multinuclear ruthenium complexes

Previous studies on butadienediyl bridged diruthenium complexes have shown that these systems constitute completely delocalized organometallic π-chromophores that defy any assignment of the redox processes as metal or ligand based [72,73]. These studies have been extended to symmetrically and unsymmetrically bridged dinuclear styryl complexes. Quantum chemical calculations in line with the analysis of experimental data give deeper insight into the electron density redistribution between the metal centers and the bridging ligands and into the degree of charge and spin delocalization within these systems.

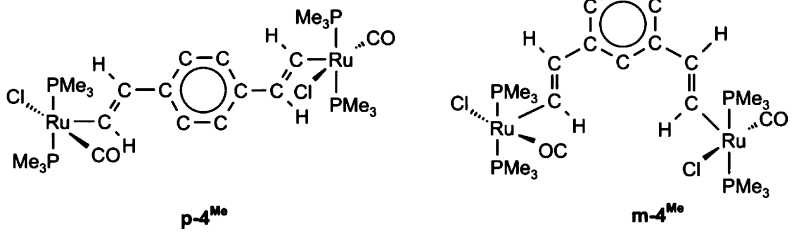

Chart 3. The *meta*- and *para*-divinylphenylene bridged diruthenium model complexes **m-4^{Me}** and **p-4^{Me}**.

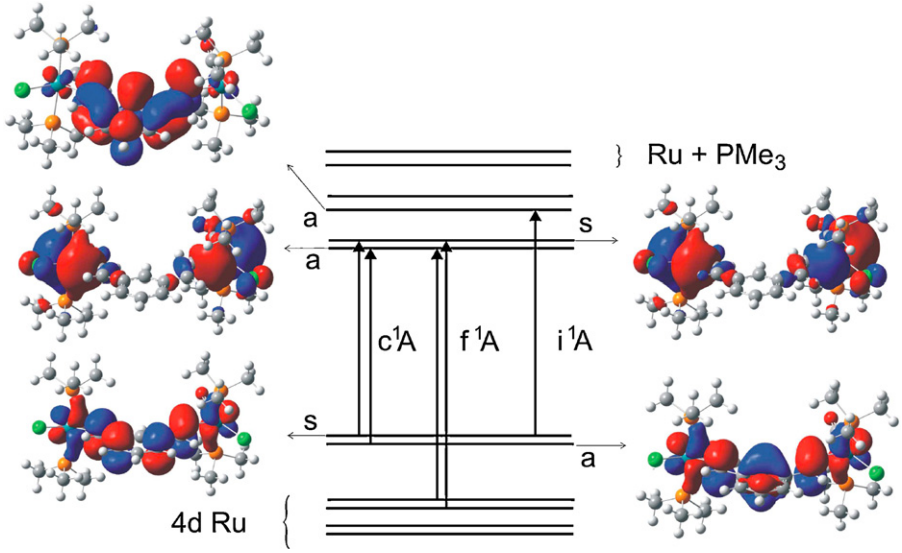

Fig. 4. Qualitative MO scheme of **m-4^{Me}** (G03/B3LYP). Arrows indicate the main contributions to the lowest allowed TD-DFT-calculated transitions. Symbols 's' and 'a' label the symmetric and antisymmetric combination of contributing 4d Ru orbitals, respectively.

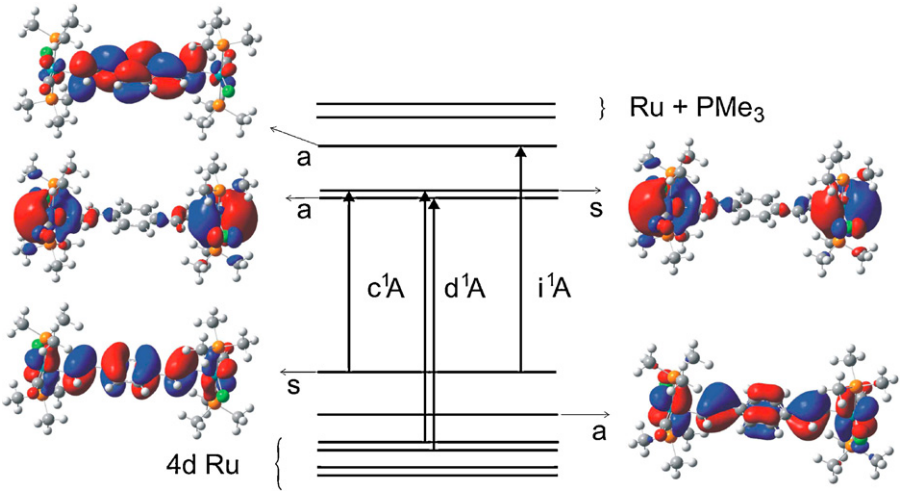

Fig. 5. Qualitative MO scheme of **p-4^{Me}** (G03/B3LYP/CPCM). Arrows indicate the main contributions to the lowest allowed TD-DFT-calculated transitions. Symbols 's' and 'a' label the symmetric and antisymmetric combination of contributing 4d Ru orbitals, respectively.

3.2.1. Divinylphenylene bridged diruthenium complexes

Divinylphenylene bridged diruthenium complexes *E,E*-[{(P^iPr_3)$_2$(CO)ClRu}$_2$(μ-HC=CH–C_6H_4–CH=CH-1,3)] (**m-4**) and *E,E*-[{(P^iPr_3)$_2$(CO)ClRu}$_2$(μ-HC=CH–C_6H_4–CH=CH-1,4)] (**p-4**) have been prepared and studied [74,75]. DFT calculations were performed on model complexes **m-4^{Me}** and **p-4^{Me}** (Chart 3) in order to compare the electronic structures of the *meta* and the *para* isomers and to explain differences in their behavior. It was shown that G03/B3LYP calculations on model system **p-4^{Me}** well describe the experimental crystal structure [76]. The good match of calculated and experimental structures also pertains to the dihedral angle of 13° between the central benzene ring and the vinyl groups of **p-4**; experimental values range from 13.3° to 15.0°.

The qualitative MO schemes of the neutral complexes and the shapes of the frontier orbitals are depicted in Figs. 4 and 5. The composition of the frontier orbitals is similar for both isomers. The HOMO and HOMO-1 levels have about 60–70% contributions from the π_3 levels of the divinylphenylene ligand interacting with the appropriate combination of metal d-orbitals (25–35%). HOMO and HOMO-1 levels are separated by 0.97 eV for **p-4^{Me}**. In the case of **m-4^{Me}**, the HOMO and HOMO-1 orbitals are nearly degenerate with an energy gap of just 0.22 eV.

TD-DFT calculations with solvent CPCM correction reasonably well described experimental UV–vis spectra of neutral complexes **m-4** and **p-4** [75]. Arrows in Figs. 4 and 5 indicate the main contributions to the lowest allowed TD-DFT-calculated transitions for the neutral **p-4^{Me}** and **m-4^{Me}** systems. Based on the composition of these orbitals, these transitions may be described as mixed bridging ligand-to-metal (LMCT) and bridging ligand-to-phosphine (LLCT) charge-transfer bands (c^1A). A transition at higher energies (f^1A in Fig. 4), which is only visible as a shoulder in the experimental spectra, has d–d character while the most intense absorption (i^1A) in the near UV can be interpreted as a $\pi \rightarrow \pi^*$ transition within the extended delocalized metal-organic chromophor.

The compositions of FMOs indicate that, upon stepwise oxidation, electrons are withdrawn from a mainly ligand based MO. The ruthenium contribution to the redox orbitals should again be reflected by shifts of the CO bands upon formation of the radical cations and the fully oxidized dications. Our previous calculations done by G03/BPW91 reproduced the experimentally observed stepwise CO-band shifts to higher energies upon sequential oxidation qualitatively well. The occurrence of one band in the neutral forms and the dications of both forms as well as just one main CO band for **p-4$^{\bullet+}$** was compatible with the computational results. The shift of the HC=CH band upon sequential oxidation was also well reproduced. A major discrepancy between calculated and experimental data, however, arose in the case of **m-4$^{\bullet+}$** in that the calculations failed to adequately reproduce the sizable splitting of the CO frequencies for the radical cation **m-4$^{\bullet+}$**. We tried to cure this discrepancy by applying the broken symmetry approach. DFT calculations with pure density functional BPW91 as well as hybrid B3LYP and PBE0 lead to a completely delocalized picture for both systems. The calculated separation of CO stretching frequencies by B3LYP and PBE0 was only about 18 cm^{-1}. It was shown that a larger admixture of Hartree-Fock (HF) exchange can help in finding the symmetry broken solution [77]. This approach (using MPW1K functional [78] with a significant HF component) was applied successfully to bis(ethynyl)carborane bridged diruthenium complexes [79]. Therefore we repeated calculations with meta-GGA density functional M05-2x [35] with 56% of HF exchange. In doing so, a symmetry broken solution was found for the radical cation **m-4$^{Me\bullet+}$**. The frequency calculation on the symmetrical **m-4$^{Me\bullet+}$** system optimized under C_2 symmetry constraints gave one imaginary frequency. The energy of the symmetrical (constrained) system is about 0.104 eV higher than that obtained for the unsymmetrical structure, the imaginary frequency corresponding to a symmetry breaking mode. In the case of **p-4$^{Me\bullet+}$** the calculations inevitably led to a delocalized state. Fig. 6 shows that in **p-4$^{Me\bullet+}$** the spin density spreads over both metal centers and the bridge. Contrary to this the spin density is localized on just one Ru–CH=CHPh subunit of **m-4$^{Me\bullet+}$**. Analogous electron density distributions were derived for corresponding purely organic *meta*-distryryl benzenes or *meta*-phenylenevinylene oligomers [80].

The comparison of experimental and DFT-calculated IR spectra (Table 1, Figs. 7 and 8) show for both complexes that the variations of the stretching frequencies $\tilde{\nu}$(CO) and $\tilde{\nu}$(C=C) with successive oxidation is now nicely reproduced by calculations. The experimentally observed separation of the CO stretches of 56 cm^{-1} of **m-4$^{\bullet+}$** is nearly identical to the calculated value of 54 cm^{-1}. For **p-4$^{\bullet+}$** calculations provide an almost degenerate set of $\tilde{\nu}$(CO), again in agreement with the experiment.

The intense EPR signals of **m-4$^{\bullet+}$** and **p-4$^{\bullet+}$** at around $g_{iso} \approx 2.028$ in fluid solution indicate that the oxidation is again a ligand dominated process. Both radical cations exhibit resolved hyperfine splittings to the vinyl protons and to the ruthenium nuclei. The slight deviations of the isotropic and average *g*-values from the free electron value g_e observed for **m-4$^{\bullet+}$** and **p-4$^{\bullet+}$** are indicative

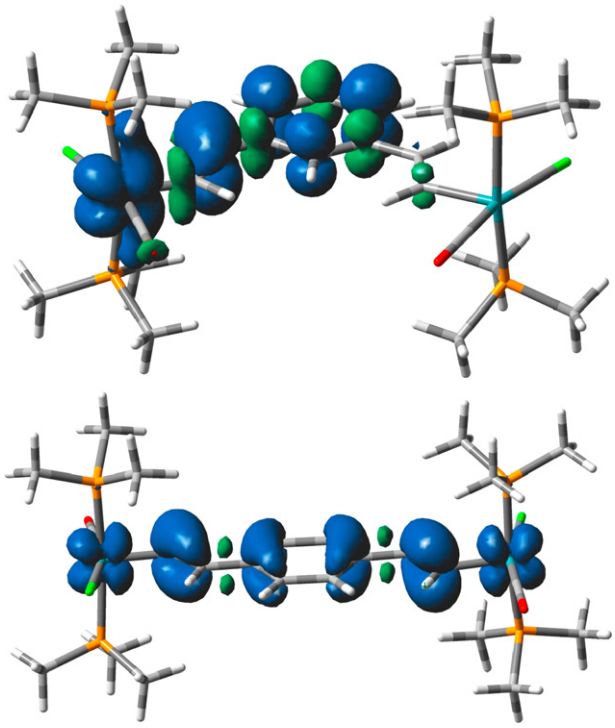

Fig. 6. DFT (G09/M05-2x) calculated spin densities for **m-4**$^{Me\bullet+}$ (top) and **p-4**$^{Me\bullet+}$ (bottom).

Table 1
Comparison of selected experimental stretching frequencies **m-4**$^{n+}$ and **p-4**$^{n+}$ with G03/M05-2x calculated ones for models **m-4**$^{Me\ n+}$ and **p-4**$^{Me\ n+}$.

	Experimental[a]			Calculated[b]		
	$\tilde{\nu}_1$(CO)	$\tilde{\nu}_2$(CO)	$\tilde{\nu}_1$(C=C)	$\tilde{\nu}_1$(CO)	$\tilde{\nu}_2$(CO)	$\tilde{\nu}$(C=C)
m-4	1910	1910	1577, 1554	1908	1912	1540
m-4^{+}	1915	1971	1524	1922	1976	1510
m-4^{2+}	1983	1983	Not detected	1994	1998	1435
p-4	1910	1910	1573, 1561	1912	1913	1540
p-4^{+}	1932[c]	1932[c]	1519, 1503, 1482	1945	1952	1462
p-4^{2+}	1991	1991	1511	1991	1995	1501

[a] Energies are given for 1,2-$C_2H_4Cl_2$ solutions in cm^{-1}.
[b] Calculated band energies scaled by the factor of 0.922.
[c] Weaker CO bands at 1942 and 1915 cm^{-1} were also observed which possibly correspond to another rotamer with less extensive charge delocalization.

of non-negligible metal contributions to the SOMOs. EPR parameters calculated for **m-4**$^{Me\bullet+}$ and **p-4**$^{Me\bullet+}$ by the ADF/BP86 approach including spin-orbit coupling agree reasonably with the experimental ones. Calculations for **m-4**$^{Me\bullet+}$ gave an isotropic g-value $g_{iso} = 2.039$ and a splitting of the g-tensor with $g_1 = 2.069$, $g_2 = 2.034$ and $g_3 = 2.016$, while the corresponding values for **p-4**$^{Me\bullet+}$ are $g_{iso} = 2.029$ and $g_1 = 2.050$, $g_2 = 2.026$ and $g_3 = 2.014$. These are to be compared with experimental values $g_{iso} = 2.0274$ for **m-4**$^{\bullet+}$ and $g_{iso} = 2.0278$ for **p-4**$^{\bullet+}$.

The different conclusions as to the electronic structure of **m-4**$^{Me\bullet+}$ and the degree of electron and spin delocalization drawn from IR and EPR spectroscopy relate to different vibrational and EPR timescales. While the radical cation of the *meta*-isomer, **m-4**$^{\bullet+}$, is clearly unsymmetrical (that is partially localized) on the vibrational timescale of 1×10^{-11} to 1×10^{-12} s, it appears to be symmetrical (that is delocalized) on the slower EPR timescale of 1×10^{-9}

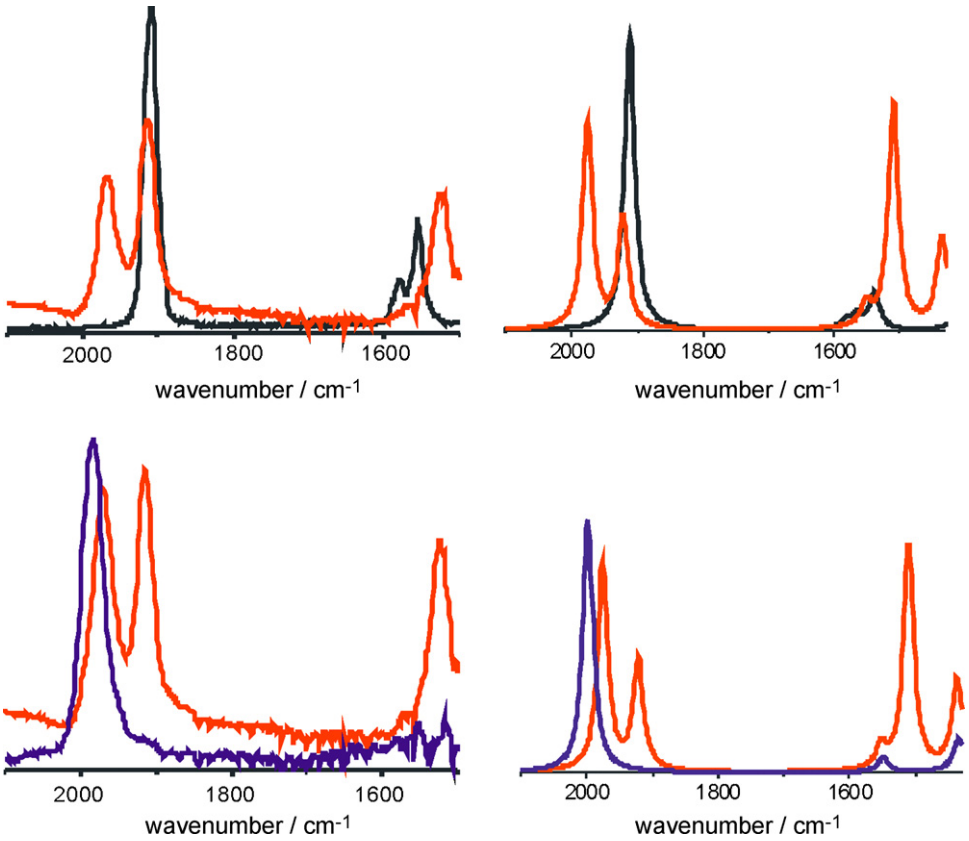

Fig. 7. Comparison of experimental and simulated IR spectra of **m-4**$^{n+}$. IR-spectroelectrochemistry of **m-4** in DCE/NBu_4PF_6 at 295 K; first oxidation (left upper graph), second oxidation (left lower graph). Simulated IR spectra (scaling factor 0.922); first oxidation (right upper graph) – black line: **m-4**^{Me}, red line: **m-4**$^{Me\bullet+}$; second oxidation (right lower graph) red line: **m-4**$^{Me\bullet+}$, blue line: **m-4**$^{Me2+}$.

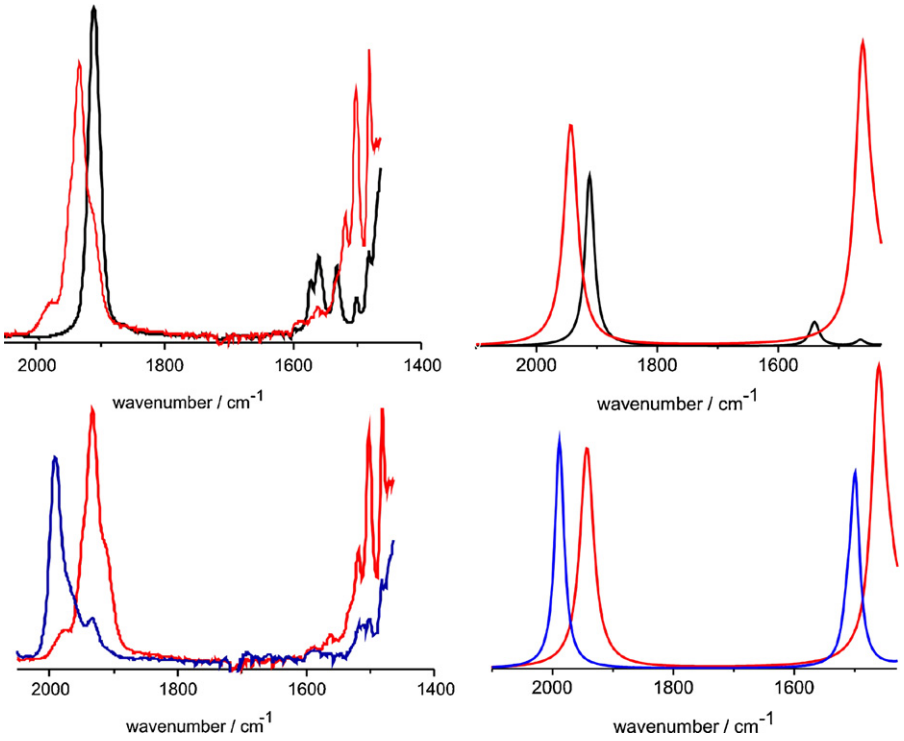

Fig. 8. Comparison of experimental and simulated IR spectra of **p-4^{n+}**. Placement of individual graphs is the same as within the caption to Fig. 7.

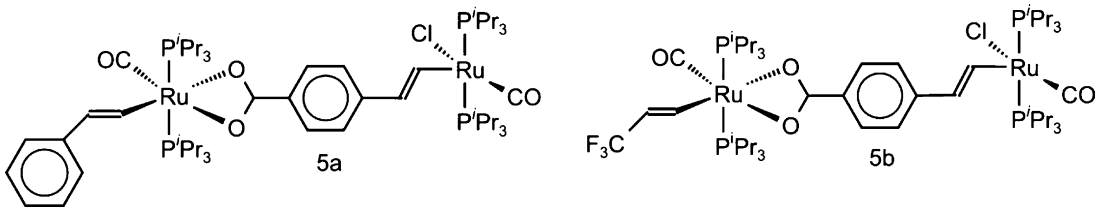

Chart 4. Vinylbenzoate bridged diruthenium complexes **5a** and **5b**.

to 1×10^{-8} s. In fact, solution EPR spectra of **m-4$^{\bullet+}$** and **p-4$^{\bullet+}$** are nearly superimposable with only slightly different hyperfine coupling constants. This parallels the phenomenon of time-dependent valence detrapping where the assignment of a mixed-valent system as either fully delocalized Class III or localized Class II depends on the timescale of the experiment [81–84]. In mixed-valent chemistry, such behavior is typical of systems that are close to the interesting borderline between these two regimes [85,86]. In the case of **m-4$^{\bullet+}$**, it may however rather indicate a time-dependent localization of charge and spin on predominantly one or delocalization over both styryl subunits.

3.2.2. Dinuclear systems with vinylbenzoate bridges

Vinylbenzoate bridged diruthenium complexes Ru(HC=CHR)(CO)(P^{i}Pr$_3$)$_2$(μ-4-OOCC$_6$H$_4$–CH=CH)RuCl(CO)(P^{i}Pr$_3$)$_2$ with substituents R = Ph (**5a**) or CF$_3$ (**5b**) (Chart 4) contain two redox-active vinyl ligands which assume either a terminal or a bridging function. This fact brings in another dimension and complicates the assignment of the individual redox sites along the redox sequences. The primary oxidation can either lead to a more delocalized structure when occurring on the bridge or to a more localized one if the terminal ligand is oxidized first. Spectroelectrochemical measurements in line with DFT calculations on simplified model complexes **5a$^{Me\ n+}$** and **5b$^{Me\ n+}$** (PMe$_3$ instead of P^{i}Pr$_3$) were performed in order to assess the respective order of redox events [87].

Owing to the inherent asymmetry of these complexes, one expects to see two different CO absorption bands for **5a$^{\bullet+}$** and **5b$^{\bullet+}$**, irrespective of the identity of the primary oxidation site. UKS calculations lead to symmetry broken solutions for both cations **5a$^{Me\bullet+}$** and **5b$^{Me\bullet+}$**. Fig. 9 shows two possible alternative valence

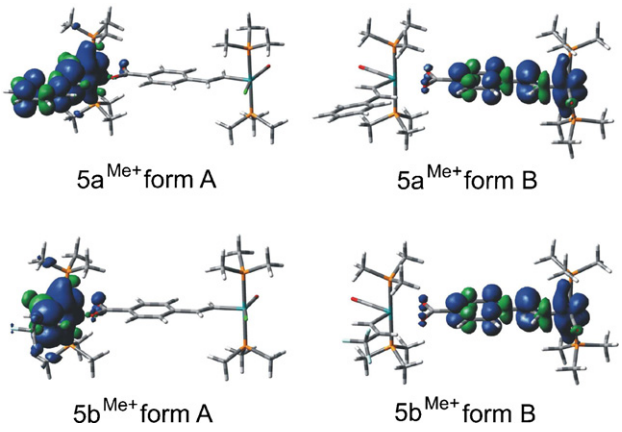

Fig. 9. DFT (G09/M05-2x) calculated spin densities for **5a$^{Me\bullet+}$** (top) and **5b$^{Me\bullet+}$** (bottom). Spin densities were calculated at optimized geometries with the exception of **5a$^{Me\bullet+}$**, form B, which was based on the frozen geometry estimated from the optimized geometry of **5b$^{Me\bullet+}$**.

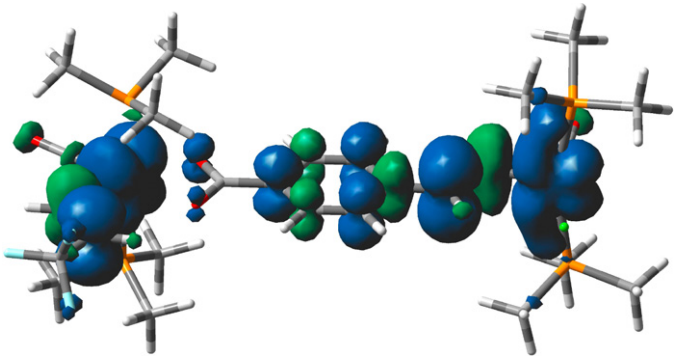

Fig. 10. DFT (G09/M05-2x) calculated spin densities for the triplet state of $\mathbf{5a^{2+}}$.

tautomeric forms differing in their charge and spin-density distributions. In form A the spin density resides on the terminal Ru(HC=CHR) unit whereas in form B the spin density is spread over the central diruthenium vinylbenzoate part. Geometry optimization of the radical cation $\mathbf{5b^{Me\bullet+}}$ indicates the form B is the most stable one, the local energy minimum was found slightly higher (ΔG = 0.029 eV) for form A. The geometry optimizations of $\mathbf{5a^{Me\bullet+}}$ found only the form A to be stable. For doubly oxidized species $\mathbf{5a^{2+}}$ and $\mathbf{5b^{2+}}$ geometry optimization indicates a completely delocalized triplet configuration (Fig. 10) as the lowest energy solution. Fig. 11 shows that vibrational analysis at the above mentioned energy minima nicely reproduce experimental IR spectra in the region of CO frequencies.

EPR parameters calculated for the mono-oxidized forms of $\mathbf{5a^{Me\bullet+}}$ and $\mathbf{5b^{Me\bullet+}}$ by the ADF/BP86 approach again agree reasonably with the experimental values. The calculated isotropic g-value g_{iso} = 2.042 and the splitting of the g-tensor with g_1 = 2.053, g_2 = 2.040 and g_3 = 2.032 for $\mathbf{5a^{Me\bullet+}}$ and g_{iso} = 2.059 and g_1 = 2.081, g_2 = 2.058 and g_3 = 2.040 for $\mathbf{5b^{Me\bullet+}}$ are comparable with experimental values g_{iso} = 2.0492 for $\mathbf{5a^{\bullet+}}$ and g_{iso} = 2.0506 for $\mathbf{5b^{\bullet+}}$. EPR spectroscopy of $\mathbf{5a^{\bullet+}}$ and $\mathbf{5b^{\bullet+}}$ in fluid solution point to vinyl ligand dominated oxidation, but argue against an oxidation process occurring on the CF_3CH=CH site of $\mathbf{5b^{Me\bullet+}}$ since the radical cation derived of its corresponding mononuclear precursor Ru(CH=CHCF$_3$)(η^2-OOCC$_6$H$_4$–C≡CH-4)(CO)(P^{i}Pr$_3$)$_2^{\bullet+}$ is EPR silent under these conditions. In line with that argument, the experimentally observed IR

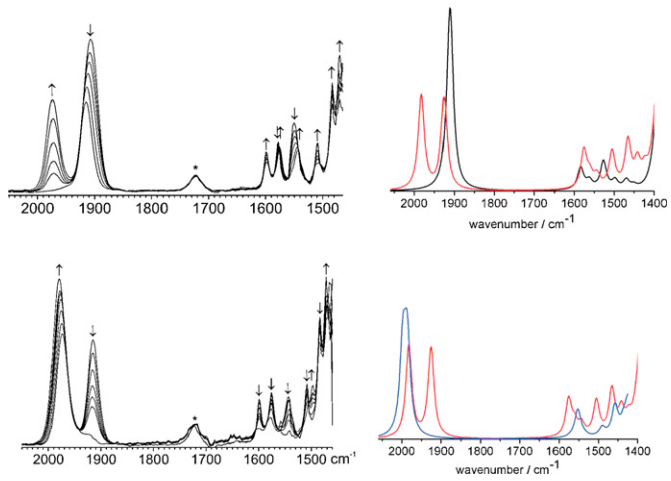

Fig. 11. Comparison of experimental and simulated IR spectra of **5a**. IR-spectroelectrochemistry of **5a** in DCE/NBu$_4$PF$_6$; first oxidation (left upper graph), second oxidation (left lower graph). Simulated IR spectra (scaling factor 0.922); first oxidation (right upper graph) – black line: **5a**, red line: $\mathbf{5a^{\bullet+}}$; second oxidation (right lower graph) red line: $\mathbf{5a^{\bullet+}}$, blue line: $\mathbf{5a^{2+}}$. A similar picture was obtained for the series of complexes $\mathbf{5b^{n+}}$.

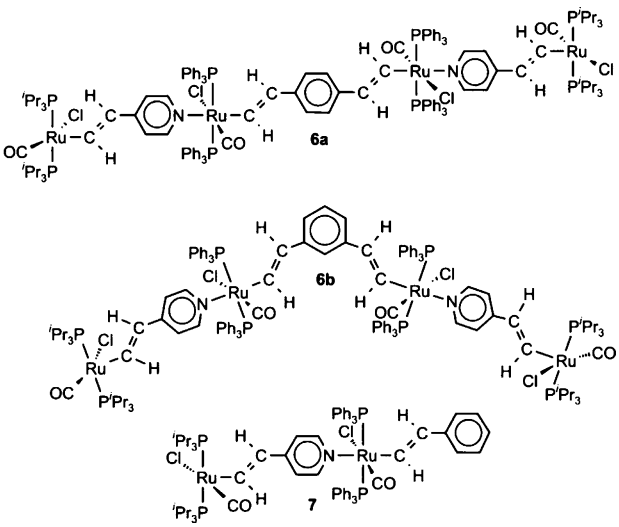

Chart 5. The divinylphenylene and vinylpyridine bridged tetraruthenium complexes **6a,b** and the dinuclear vinylpyridine bridged styryl complex **7**.

CO-band shifts of $\mathbf{5a/5a^{\bullet+}}$ and of $\mathbf{5b/5b^{\bullet+}}$ closely resemble those observed for the Ru(CH=CHPh)(OOCC$_6$H$_4$C≡CH)(CO)(P^{i}Pr$_3$)$_2^{0/\bullet+}$ couple or the RuCl(CH=CHPh)(CO)(P^{i}Pr$_3$)$_2^{0/\bullet+}$ one that resemble the terminal site of **5a** or the briding one of **5b**.

3.2.3. Tetraruthenium complexes bridged by phenylenevinylene and vinylpyridine ligands

Tetranuclear complexes {(P^{i}Pr$_3$)$_2$(CO)ClRu(μ-CH=CHpy)(CO)Cl(PPh$_3$)$_2$Ru}$_2$(μ-CH=CH–C$_6$H$_4$–CH=CH-1,4 or -1,3) (**6a,b**) (Chart 5) with vinylpyridine ligands connecting peripheral five-coordinated P^{i}Pr$_3$ substituted vinyl ruthenium units to a central divinylphenylene bridged diruthenium core have been prepared and investigated [88]. Both complexes undergo a series of five consecutive redox processes that come as a pair of moderately split (by ca. 230 and 300 mV for complexes **6a** and **6b**) one-electron waves, an unresolved two-electron wave and an additional one-electron oxidation. The wave splittings of the first two waves of **6a,b** closely match those of the dinuclear complexes {(4-EtOOC–C$_5$H$_3$N)(PPh$_3$)$_2$(CO)ClRu}$_2$(μ-CH=CH–C$_6$H$_4$–CH=CH)-1,3 or -1,4 that represent the core section of complexes **6a,b** [74]. That particular splitting pattern is strongly suggestive of a redox sequence where the core divinylphenylene bridged diruthenium unit is oxidized first in the same stepwise manner as was observed for pentacoordinated diruthenium complexes **m-4** and **p-4** and the related hexacoordinated derivatives {(4-EtOOC–C$_5$H$_3$N)(PPh$_3$)$_2$(CO)ClRu}$_2$(μ-CH=CH–C$_6$H$_4$–CH=CH)-1,3 or -1,4 featuring additional pyridine ligands. The following two-electron wave arises from the simultaneous oxidation of the peripheral vinylpyridine appended sites which obviously do not interact with each other via the central oxidized divinylphenylene bridged diruthenium unit. The fifth oxidation probably again relates to the central portion of this molecule.

Results from IR-spectroelectrochemical studies further substantiate the proposed order of redox events. Neutral **6a** has a broad CO band that can be deconvoluted into two separate absorptions at 1924 and 1919 cm^{-1} for the inherently different peripheral and internal {RuCl(CO)(PR$_3$)$_2$(CH=CHR′)} subunits. Gradual oxidation of **6a** to $\mathbf{6a^{\bullet+}}$ and then to $\mathbf{6a^{2+}}$ first leads to the development of a high-energy shoulder at 1934 cm^{-1} (see Fig. 12) and then to a distinct two band pattern with CO-band positions of 1979 and 1934 cm^{-1}. This is highly reminiscent of the $\mathbf{p\text{-}4^{0/\bullet+/2+}}$ and the even closer related {(4-EtOOC–C$_5$H$_3$N)(PPh$_3$)$_2$(CO)ClRu}$_2$(μ-CH=CH–C$_6$H$_4$–CH=CH)-

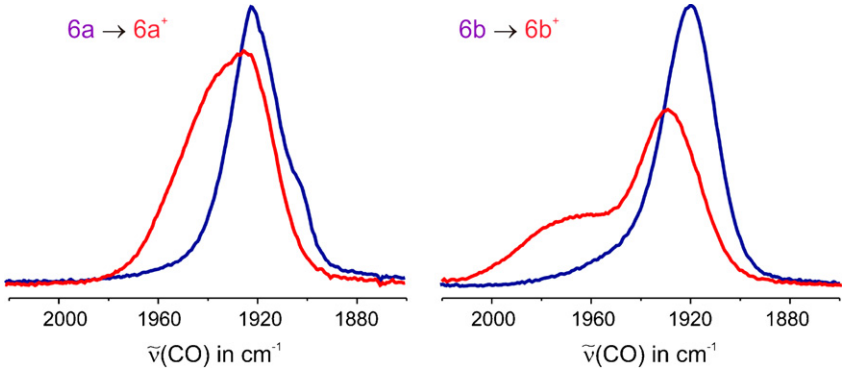

Fig. 12. Comparison of the IR spectra of **6a/6a•+** and **6b/6b•+**.

$1,4^{0/\bullet+/2+}$ series, where one-electron oxidation first produced a single CO band with a moderate shift of 13 cm^{-1} with respect to the neutral (1926 $cm^{-1} \rightarrow$ 1939 cm^{-1}) and then a significantly larger shift of 33 cm^{-1} (1939 $cm^{-1} \rightarrow$ 1972 cm^{-1}) upon the second oxidation (see Fig. 8, the lower energy CO-band of **p-4^{2+}** originates from the peripherally appended sites). For **6b**, the first oxidation produced a two band pattern with a weaker absorption at a significantly higher energy of 1964 cm^{-1} and the main band at a similar position as in the neutral (see Fig. 12). This relates to a more localized electronic structure of the divinylphenylene bridged diruthenium unit having the *meta* topology (see Section 3.2 of this paper).

Quantum chemical calculations on simplified model complexes **6a^{Me}** and **6b^{Me}** agree with this picture and explain the lack of eletronic interactions between the two vinylpyridine appended terminal sites through the central divinylphenylene bridges. The occupied FMOs HOMO to HOMO-6 of the neutrals are either delocalized across the central divinylphenylene part of complexes **6a,b** (HOMO and HOMO-1, see Fig. 13) or combinations of orbitals centered on the individual {RuCl(CO)$(PR_3)_2$} metal sites of that unit. The first occupied FMO with dominant contributions of the outer vinylpyridine ruthenium sites appears as HOMO-7, 1.7 eV (**6a^{Me}**) or 1.4 eV (**6b^{Me}**) below the HOMO. Calculated spin densities for radical cations **6a$^{\bullet+}$** and **6b$^{\bullet+}$** agree with electron removal from the respective HOMO of the neutrals upon one-electron oxidation and faithfully retrace the shapes of the immediate occupied frontier level [88]. Neither of the vinyl ligand based orbitals delocalize beyond the inner ruthenium atoms. This prevents charge and spin delocalization onto the outer vinylpyridine ruthenium {$(PR_3)_2$(CO)ClRu(CH=CH-py)} subunits, and, as a consequence, prevents electronic coupling between the individual vinylpyridine units. The same situation pertains to the simpler vinylpyridine bridged diruthenium complex $(P^iPr_3)_2$(CO)ClRu(CH=CH-py)RuCl(CH=CHPh)$(PPh_3)_2$Cl, **7**. This suggests that, with the appropriate choice of {Ru} and {Ru′} such as to direct the primary oxidation to the bridging vinylpyridine ligand and the attached metal sites, oligomers {Ru}[(py-CH=CH){Ru′}]$_n$ might be electrically conducting at low doping (*i.e.* low oxidation) levels.

4. Tetraruthenium complexes with TCNX bridging ligands

4.1. The oxidation of a tetrakis(4-styryl)ethene (TSTE) bridged tetraruthenium complex

A tetraruthenium complex with four equivalent ruthenium moieties bridged by the tetrakis(4-styryl)ethene ligand (TSTE) [{$(P^iPr_3)_2$(CO)ClRu(μ_4-CH=CH–C_6H_4)}$_4$(C=C)], **8** (Chart 6), undergoes a series of one-electron oxidations (**8** ⇄ **8$^{\bullet+}$** ⇄ **8^{2+}** ⇄ **8$^{\bullet3+}$** ⇄ **8^{4+}**) which primarily involve the organic ligand [89]. These oxidations come as pairs of two closely spaced one-electron processes with rather small comproportionation constants. Despite the fact that the intermediate odd-electron species **8$^{\bullet+}$** and **8$^{\bullet3+}$** only coexist in equilibrium with their neighbouring closed-shell reduced and fully oxidized redox congeners **8** and **8^{2+}** or **8^{2+}** and **8^{4+}**, respectively, their presence was clearly indicated by virtue of their characteristic electronic absorption bands that extend into the high-energy regime of the mid-IR. These extremely low-energy bands first grow in and then diminish upon traversing the composite **8$^{0/\bullet+/2+}$** or **8$^{2+/\bullet3+/4+}$** waves. Calculations on model complexes **8$^{Me\ n+}$** rationalize and retrace the variation of the electronic spectra for the thermodynamically stable members of the redox series **8^{Me}** ⇄ **8$^{Me\ 2+}$** ⇄ **8$^{Me\ 4+}$**.

Fig. 14 depicts the HOMO and HOMO-1 of the neutral complex. Both are mainly composed of π-orbitals of the TSTE bridge.

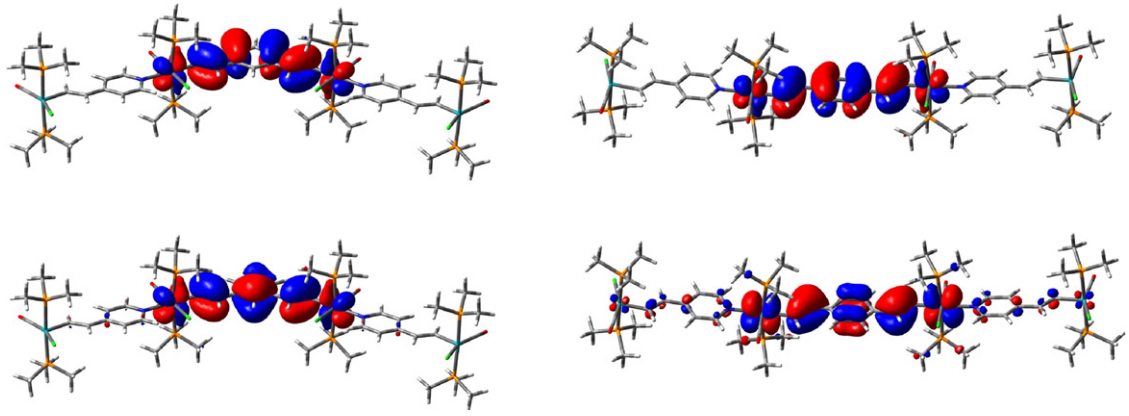

Fig. 13. Contour plots of HOMO (top) and HOMO-1 (bottom) of the model complexes **6a^{Me}** (left) and **6b^{Me}** (right).

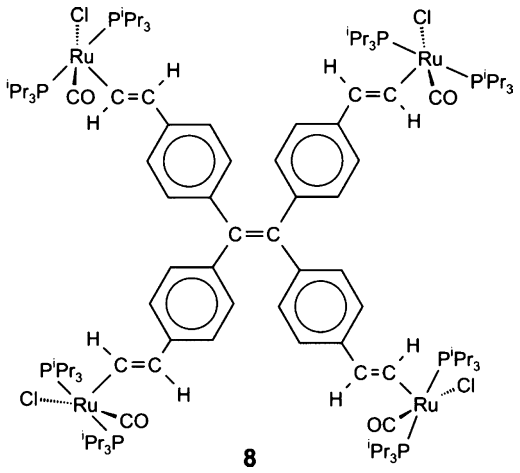

Chart 6. The TSTE bridged tetraruthenium complex **8**.

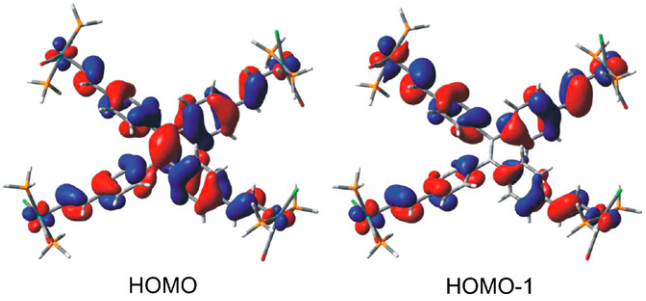

Fig. 14. Contour plots of HOMO and HOMO-1 of the model complex $\mathbf{8^{Me}}$.

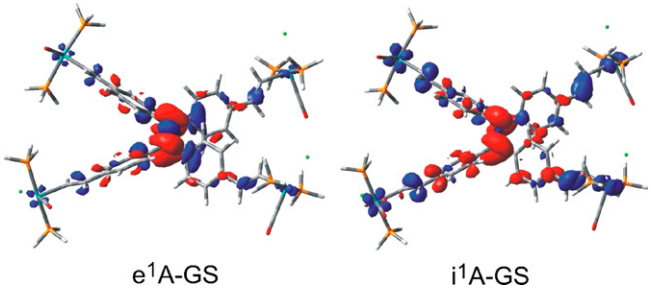

Fig. 16. DFT-calculated electron density differences between the excited and ground states of $\mathbf{8^{Me}}$ corresponding to the intense transitions. Red and blue areas correspond to increasing and diminishing electron densities, respectively.

In the course of stepwise oxidation up to the tetracation level electrons are stepwise withdrawn from these orbitals. The HOMO and HOMO-1 orbitals of **8** thus form the LUMO and HOMO of doubly oxidized $\mathbf{8^{Me\,2+}}$.

The comparison of experimental and TD-DFT simulated electronic spectra of the neutral complex and its oxidized dication depicted in Fig. 15 shows that calculations describe the spectrum of neutral **8** and the appearance of new intense features in the visible and NIR regions for doubly oxidized $\mathbf{8^{2+}}$ well. Although the energies of the low lying excitations are slightly overestimated, the TD-DFT calculations retrace the main features of the experimental spectra. Figs. 16 and 17 display the calculated electron density differences corresponding to the intense transitions within the neutral and doubly oxidized forms of model complex $\mathbf{8^{Me}}$. Fig. 16 indicates that intense features in neutral $\mathbf{8^{Me}}$ correspond to intraligand charge-transfer (ILCT) e^{1}A and i^{1}A transitions with appreciable MLCT character for the latter. Intense low-energy transitions b^{1}A and d^{1}A in $\mathbf{8^{Me\,2+}}$ correspond mainly to the HOMO → LUMO and HOMO-2 → LUMO excitations, respectively. The composite low-

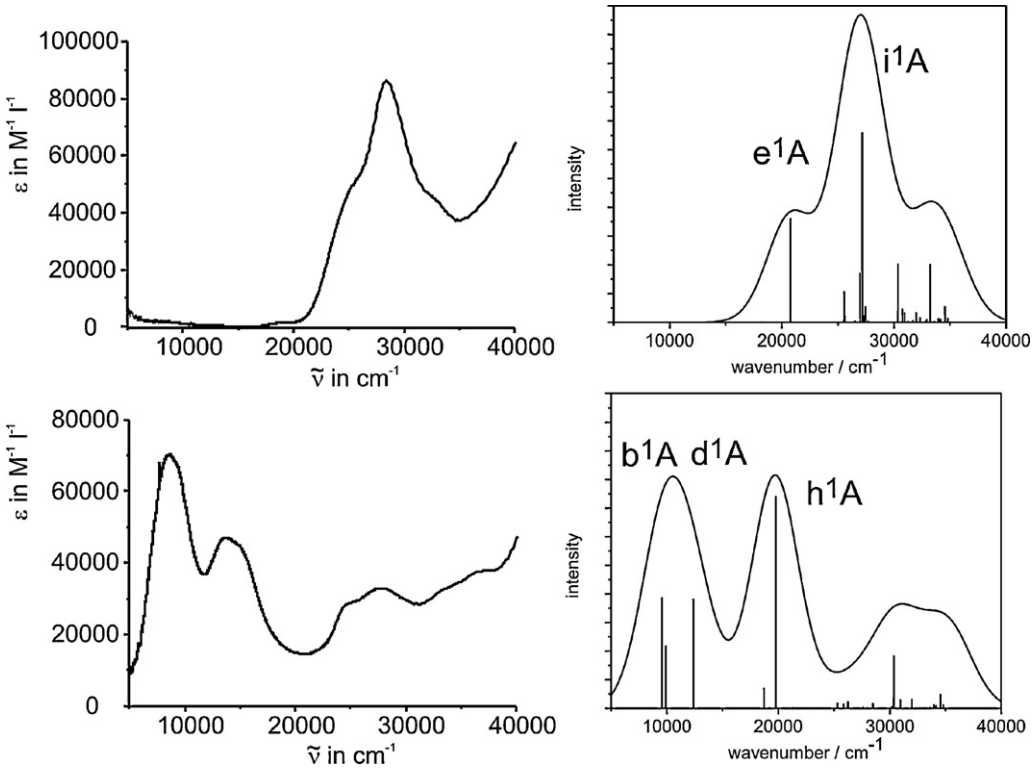

Fig. 15. Comparison of experimental and simulated UV–vis spectra of **8**. UV–vis–near-IR-spectroelectrochemistry of complex **8** in 1,2-$C_2H_4Cl_2$/NBu_4PF_6. Spectroscopic changes upon oxidation: neutral complex (left upper graph), doubly oxidized species $\mathbf{8^{2+}}$ (left lower graph). Simulated spectra: neutral complex $\mathbf{8^{Me}}$ (right upper graph), doubly oxidized species $\mathbf{8^{Me2+}}$ (right lower graph).

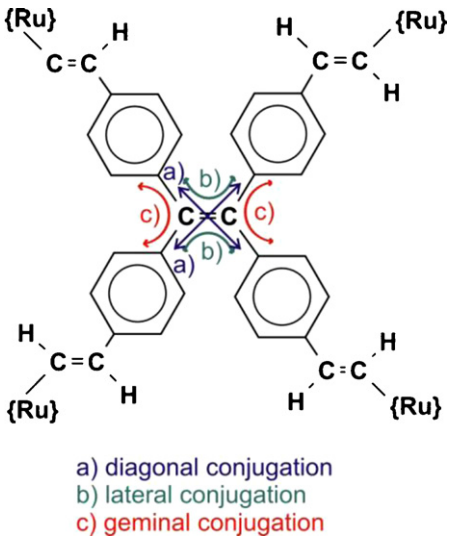

Chart 7. The three different conjugation pathways for cross-conjugated $\mathbf{8}^{n+}$.

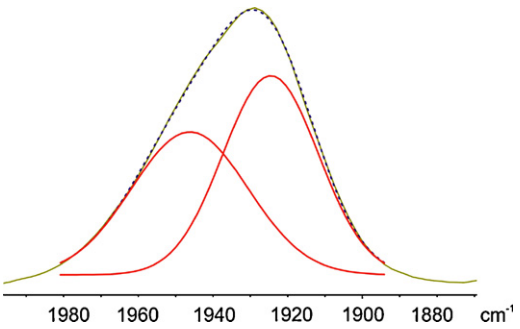

Fig. 18. Comparison of the experimental (green olive line) and the simulated (blue dotted line) ν(CO) band of $\mathbf{8}^{2+}$ as obtained by spectral deconvolution into the two individual bands shown in red.

energy band at around 10,000 cm^{-1} can thus be characterized as involving both LLCT and MLCT transitions. The band h^1A calculated at around 19,000 cm^{-1} is assigned to the HOMO-1 → LUMO + 1 excitation and has also mixed LLCT and MLCT character.

Another interesting aspect of this work relates to the general problem of π-conjugation in cross-conjugated systems like $\mathbf{8}^{n+}$. Tetraphenylethenes offer three different pathways of electron conjugation which are denoted as diagonal, lateral and geminal (see Chart 7). There is a long-standing debate on how efficient each of these pathways is and on which is the dominant one for each of the various oxidation states [90–93]. This is coupled with the question of the degree and timescale of charge (or spin) equilibration in such systems. In its IR-spectrum dioxidized $\mathbf{8}^{2+}$ displays an unsymmetrical and broadened CO band for its individual $Ru(CO)Cl(P^iPr_3)_2$ moieties that was deconvoluted into separate peaks located at 1942 and 1924 cm^{-1} with an excellent fit between the experimental and simulated spectrum (Fig. 18). This essentially means that there are two distinct pairs of IR active $Ru(CO)Cl(P^iPr_3)_2$ tags that differ in their intrinsic electron densities. This in turn means that just one out of the three different pathways of electron delocalization is effective on the short vibrational timescale (note that any combination of two effective pathways would render all four of these subunits electronically equivalent).

Quantum chemical calculations on the simplified model with PH_3 instead of P^iPr_3 ligands reproduce the general CO-band shift upon stepwise oxidation from **8** to $\mathbf{8}^{2+}$ and finally to $\mathbf{8}^{4+}$ qualitatively well [89]. The contour plot of the HOMO of $\mathbf{8}^{2+}$ which is essentially the HOMO-1 of its neutral precursor **8**, suggests that the geminal pathway is the most favorable one for conjugation in dioxidized $\mathbf{8}^{2+}$. This is mainly because dioxidation depopulates the HOMO orbital which is bonding across the central C=C double bond interconnecting the two di(styryl)methylene diruthenium groups. The calculated lengthening of that bond by nearly 0.09 Å from 1.371 Å in **8** to 1.458 Å in $\mathbf{8}^{2+}$ (PH_3 model complex) bears clear witness to this notion, as does the structural comparison of the reduced neutral and mono- or dioxidized forms of related donor substituted tetraphenylethenes [91,94,95]. While this particular result still awaits further experimental substantiation from the investigation of the three positional isomers of diruthenium di(styryl)diphenylethene complexes, we note that recent quantum chemical studies on acyclic cross-conjugated systems make a strong case of large electric conductance of their oxidized forms via the geminal pathway [96].

4.2. The formation of the dimer-of-(mixed-valent dimers) configuration in tetranuclear $\{(\mu_4\text{-TCNX})[Ru(NH_3)_5]_4\}^{8+}$, TCNX = TCNE or TCNQ

DFT calculations of the complex ions $\{(\mu_4\text{-TCNX})[Ru(NH_3)_5]_4\}^{n+}$, $n = 8$, 7 and 6; TCNX = tetracyanoethene (TCNE) or 7,7,8,8-tetracyano-*p*-quinodimethane (TCNQ), were performed in order to point out the geometric and electronic factors influencing the properties of these systems [97].

For both $\{(\mu_4\text{-TCNX})[Ru(NH_3)_5]_4\}^{8+}$ complexes the geometry optimizations by the G03/B3LYP methodology confirm [98] lowest lying triplet states, the calculated triplet-singlet separation being 0.178 eV for $\{(\mu_4\text{-TCNE})[Ru(NH_3)_5]_4\}^{8+}$ and 0.072 eV for $\{(\mu_4\text{-TCNQ})[Ru(NH_3)_5]_4\}^{8+}$. Fig. 19 illustrates the twist between the Ru–N≡C–C–C≡N–Ru moieties in the lowest lying triplet state of $\{(\mu_4\text{-TCNX})[Ru(NH_3)_5]_4\}^{8+}$ complexes.

In all cases the Ru–N≡C–C–C≡N–Ru moieties with the malonodinitrilato bridges were calculated as being close to planar, and the penta-ammineruthenium complex fragments were found to adopt a staggered conformation with respect to that plane (Fig. 19). The bonds within the Ru–N≡C–C–C≡N–Ru entities correspond to the expected values for conjugated malonodinitrilato anions bridging

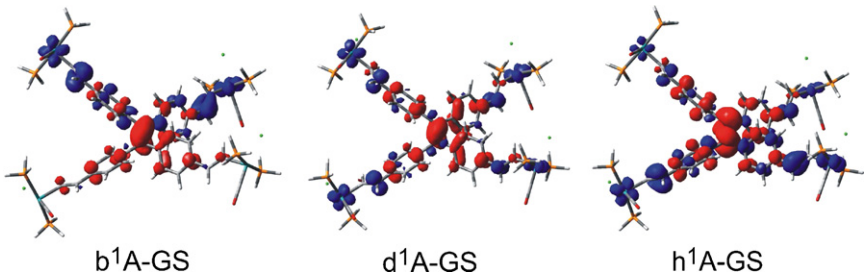

Fig. 17. DFT-calculated electron density differences between the excited and ground states of $\mathbf{8}^{Me\ 2+}$ corresponding to the intense transitions. Red and blue areas correspond to increasing and diminishing electron densities, respectively.

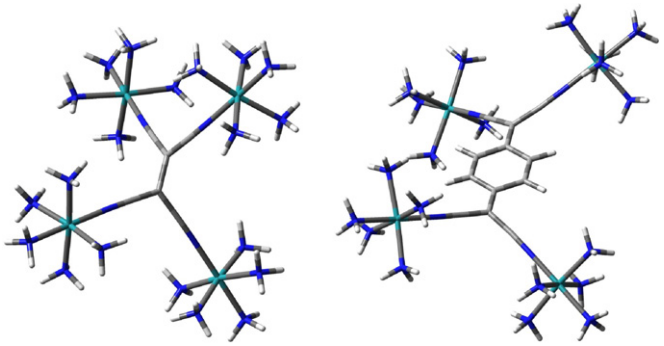

Fig. 19. G03/B3LYP optimized structures of the molecular ions $\{(\mu_4\text{-TCNX})[Ru(NH_3)_5]_4\}^{8+}$ (left) and $\{(\mu_4\text{-TCNX})[Ru(NH_3)_5]_4\}^{8+}$ (right) in the ^3A ground state.

two delocalized mixed-valent metal centers [98–100]. The resulting situation involving weak interaction between two strongly coupled malonodinitrilato-bridged $Ru^{2.5}Ru^{2.5}$ entities (Class III) agrees with the experimental results. The near orthogonality of the individual Ru–N≡C–C–C≡N–Ru subunits found for the ground states of the molecular ions explains the observed magnetic exchange coupling between two S = 1/2 sites and the reversible two-electron oxidation [101]. This formulation involves unconventional mixed-valent tetranuclear compounds, *i.e.* weakly coupled pairs of strongly coupled dinuclear moieties.

EPR measurements on the one electron reduced complex $\{(\mu_4\text{-TCNE})[Ru(NH_3)_5]_4\}^{7+}$ in methanol gave a rather small *g* anisotropy at $g_1 = 2.023$, $g_2 = 2.013$ and $g_3 = 1.989$. ADF/BP calculations for $\{(\mu_4\text{-TCNE})[Ru(NH_3)_5]_4\}^{7+}$ yielded a larger anisotropy due to the overestimation of the metal contribution. The inclusion of solvent influence modeled by the CPCM (G03) or COSMO (ADF) approaches leads to a much smaller angle between the Ru–N≡C–C–C≡N–Ru planes (to around 10°) in comparison to the calculation for unsolvated species. Accordingly, the Ru contributions to the SOMO for $\{(\mu_4\text{-TCNE})[Ru(NH_3)_5]_4\}^{7+}$ in solution diminish and the calculated values $g_1 = 2.030$, $g_2 = 2.017$, $g_3 = 1.986$ and $g_{iso} = 2.011$ satisfactorily describe the experimental results.

5. Conclusions

The presence of redox-active metal ions and redox-active ligands within the same complex generates considerable ambiguity about the identity of the individual redox sites and the corresponding composition of redox orbitals. Redox-active ligands may strongly contribute to or even dominate redox processes even if the intrinsic redox potentials of corresponding metal entities and the isolated ligand seem sufficiently apart. The present account summarizes our recent work on mononuclear and symmetrically or unsymmetrically bridged di- and tetranuclear ruthenium complexes of vinyl and TCNX ligands and provides new views on the electron density redistribution in radical ions using the symmetry broken approach. DFT calculations enables us to identify the primary redox site as well as the charge and spin distribution between the individual components, and point out energetically close valence tautomers. The proper description of the redox processes thus requires an integrated approach that combines calculations with various spectroscopic techniques, each operating at its own intrinsic timescale [84], thus capitalizing on the various charge- or spin-sensitive labels offered by the particular system under study. The generally close correspondence between experimental and quantum chemical results demonstrates that modern quantum chemistry has grown into a powerful tool to address issues like ligand non-innocence and electron or spin delocalization in more extended arrays comprising more than just one such metal/ligand unit in their various oxidation states. IR, UV–vis–NIR profiles of closed- and open-shell systems as well as EPR parameters for the latter ones can now be calculated with good confidence. This eventually renders these calculations predictive such that they serve as a guideline for the interpretation of experimental data and for resolving remaining ambiguities.

Acknowledgements

Support from the DFG, EU (COST action D35, also supported by the Ministry of Education of the Czech Republic – grants OC 139 and 1P05OC068) and financial support by the Grant Agency of the Academy of Sciences of the Czech Republic (SZ, grant KAN100400702) is gratefully acknowledged. The experimental work in RFW's labs was generously supported by research grants from Deutsche Forschungsgemeinschaft DFG (grants Wi 1272/7-1 and 1272/7-2). RFW also wishes to thank the PhD students Michael Linseis, Jörg A. Maurer, Jörg Maurer and Florian Pevny that have been involved in this project for their dedicated work.

References

[1] A.B.P. Lever, E.S. Dodsworth, in: E.I. Solomon, A.B.P. Lever (Eds.), Inorganic Electronic Structure and Spectroscopy, Volume II: Applications and Case Studies, John Wiley & Sons, Inc., 1999, p. 227.
[2] A. Vlček Jr., S. Záliš, Coord. Chem. Rev. 251 (2007) 258.
[3] F. Neese, Coord. Chem. Rev. 253 (2009) 526.
[4] H. Chermette, Coord. Chem. Rev. 178–180 (1998) 699.
[5] W. Koch, M.C. Holthausen, A Chemist's Guide to Density Functional Theory, Wiley-VCH, Weinheim, 2000.
[6] P. Comba, M. Kerscher, Coord. Chem. Rev. 253 (2009) 564.
[7] W. Kohn, A.D. Becke, R.G. Parr, J. Phys. Chem. 100 (1996) 12974.
[8] P.E.M. Siegbahn, J. Biol. Inorg. Chem. 11 (2006) 695.
[9] P.E.M. Siegbahn, T. Borowski, Acc. Chem. Res. 39 (2006) 729.
[10] A.V. Marchenko, H. Gérard, O. Eisenstein, K.G. Caulton, New J. Chem. 25 (2001) 1382.
[11] A.V. Marchenko, H. Gérard, O. Eisenstein, K.G. Caulton, New. J. Chem. 25 (2001) 1244.
[12] A.F. Hill, M.I. Bruce, in: D.E. Shriver (Ed.), Comprehensive Organometallic Chemistry, vol. II, Pergamon, Oxford, 1995, p. 399.
[13] A. Pedersen, M. Tilset, K. Folting, K.G. Caulton, Organometallics 14 (1995) 875.
[14] J.S. Miller, Angew. Chem. Int. Ed. Engl. 45 (2006) 2508.
[15] W. Kaim, M. Moscherosch, Coord. Chem. Rev. 129 (1994) 157.
[16] G. Wang, H. Zhu, J. Fan, C. Slebodnick, G.T. Yee, Inorg. Chem. 45 (2006) 1406.
[17] J.S. Miller, A.J. Epstein, Coord. Chem. Rev. 207 (2000) 651.
[18] H. Miyasaka, C.S. Campos-Fernández, R. Clérac, K.R. Dunbar, Angew. Chem. Int. Ed. Engl. 39 (2000) 3831.
[19] M.L. Taliaferro, M.S. Thorum, J.S. Miller, Angew. Chem. Int. Ed. Engl. 45 (2006) 5326.
[20] M.J. Frisch, G.W. Trucks, H.B. Schlegel, G.E. Scuseria, M.A. Robb, J.R. Cheeseman, J.J.A. Montgomery, T. Vreven, K.N. Kudin, J.C. Burant, J.M. Millam, S.S. Iyengar, J. Tomasi, V. Barone, B. Mennucci, M. Cossi, G. Scalmani, N. Rega, G.A. Petersson, H. Nakatsuji, M. Hada, M. Ehara, K. Toyota, R. Fukuda, J. Hasegawa, M. Ishida, T. Nakajima, Y. Honda, O. Kitao, H. Nakai, M. Klene, X. Li, J.E. Knox, H.P. Hratchian, J.B. Cross, V. Bakken, C. Adamo, J. Jaramillo, R. Gomperts, R.E. Stratmann, O. Yazyev, A.J. Austin, R. Cammi, C. Pomelli, J.W. Ochterski, P.Y. Ayala, K. Morokuma, G.A. Voth, P. Salvador, J.J. Dannenberg, V.G. Zakrzewski, S. Dapprich, A.D. Daniels, M.C. Strain, O. Farkas, D.K. Malick, A.D. Rabuck, K. Raghavachari, J.B. Foresman, J.V. Ortiz, Q. Cui, A.G. Baboul, S. Clifford, J. Cioslowski, B.B. Stefanov, G. Liu, A. Liashenko, P. Piskorz, I. Komaromi, R.L. Martin, D.J. Fox, T. Keith, M.A. Al-Laham, C.Y. Peng, A. Nanayakkara, M. Challacombe, P.M.W. Gill, B. Johnson, W. Chen, M.W. Wong, C. Gonzalez, J.A. Pople, Gaussian 03, Revision E.01, Gaussian, Inc., Wallingford, CT, 2004.
[21] C. Fonseca Guerra, J.G. Snijders, G. te Velde, E.J. Baerends, Theor. Chim. Acta 99 (1998) 391.
[22] D. Andrae, U. Haeussermann, M. Dolg, H. Stoll, H. Preuss, Theor. Chim. Acta 77 (1990) 123.
[23] J.M.L. Martin, A. Sundermann, J. Chem. Phys. 114 (2001) 3408.
[24] P.C. Hariharan, J.A. Pople, Theor. Chem. Acc. 28 (1973) 213.
[25] W.J. Hehre, R. Ditchfield, J.A. Pople, J. Chem. Phys. 56 (1972) 2257.
[26] T.H. Dunning Jr., J. Chem. Phys. 90 (1989) 1007.
[27] T.H. Dunnning Jr., P.J. Hay, in: H.F. Schaefer III (Ed.), Modern Theoretical Chemistry, Plenum, New York, 1976, p. 1.
[28] D.E. Woon, T.H. Dunning Jr., J. Chem. Phys. 98 (1993) 1358.
[29] A.D. Becke, Phys. Rev. A 38 (1988) 3098.
[30] J.P. Perdew, Phys. Rev. B 33 (1986) 8822.
[31] J.P. Perdew, Y. Wang, Phys. Rev. B 46 (1992) 13244.
[32] A.D. Becke, J. Chem. Phys. 98 (1993) 5648.
[33] C. Adamo, V. Barone, J. Chem. Phys. 110 (1999) 6158.

[34] J.P. Perdew, K. Burke, M. Ernzerhof, Phys. Rev. Lett. 77 (1996) 3865.
[35] Y. Zhao, N.E. Schultz, D.G. Truhlar, J. Chem. Theor. Comput. 2 (2006) 364.
[36] Y. Zhao, D.G. Truhlar, Acc. Chem. Res. 41 (2008) 157.
[37] C.W. Murray, G.J. Laming, N.C. Handy, Amos. Chem. Phys. Lett. 199 (1992) 551.
[38] J. Neugebauer, B.A. Hess, J. Chem. Phys. 118 (2003) 7215.
[39] M.W. Wong, Chem. Phys. Lett. 256 (1996) 391.
[40] F. Neese, Spring Meeting of the European-Materials-Research-Society (EMRS), Strasbourg, France, 2003, p. 781.
[41] G. Jonkers, C.A. Delange, L. Noodleman, E.J. Baerends, Mol. Phys. 46 (1982) 609.
[42] L. Noodleman, J. Chem. Phys. 74 (1981) 5737.
[43] L. Noodleman, E.R. Davidson, Chem. Phys. 109 (1986) 13.
[44] R. Seeger, J.A. Pople, J. Chem. Phys. 66 (1977) 3045.
[45] M.E. Casida, in: D.P. Chong (Ed.), Advances in Density Functional Methods, World Scientific, Singapore, 1995, p. 155.
[46] M. Cossi, N. Rega, G. Scalmani, V. Barone, J. Comput. Chem. 24 (2003) 669.
[47] J. Tomasi, B. Mennucci, R. Cammi, Chem. Rev. 105 (2005) 2999.
[48] M.E. Casida, A. Ipatov, F. Cordova, Time-Dependent Density-Functional Theory, in: M.A.L. Marques, C. Ullrich, F. Nogueira, A. Rubio, E.K.U. Gross (Eds.), Lecture Notes in Physics, Springer, Berlin, 2006, p. 243.
[49] S. ADF2006.01-2008.01, in: Theoretical Chemistry, Vrije Universiteit, Amsterdam, The Netherlands.
[50] G. te Velde, F.M. Bickelhaupt, E.J. Baerends, C. Fonseca Guerra, S.J.A. van Gisbergen, J.G. Snijders, T. Ziegler, J. Comput. Chem. 22 (2001) 931.
[51] E. van Lenthe, A.E. Ehlers, E.J. Baerends, J. Chem. Phys. 110 (1999) 8943.
[52] E. van Lenthe, A. van der Avoird, P.E.S. Wormer, J. Chem. Phys. 108 (1998) 4783.
[53] E. van Lenthe, A. van der Avoird, P.E.S. Wormer, J. Chem. Phys. 107 (1997) 2488.
[54] A. Klamt, V. Jones, J. Chem. Phys. 105 (1996) 9972.
[55] A. Klamt, G. Schüürmann, J. Chem. Soc., Perkin Trans. 2 (1993) 799.
[56] M. Krejčík, M. Daněk, F. Hartl, J. Electroanal. Chem. 317 (1991) 179.
[57] R.L. McCreery, in: B.W. Rossiter, J.F. Hamilton (Eds.), Physical Methods of Chemistry, vol. II, John Wiley & Sons, New York, 1986.
[58] R.F. Winter, in: W. Kaim, A. Klein (Eds.), Spectroelectrochemistry, RSC Publishing Cambridge, Cambridge, 2008.
[59] S.P. Best, S.J. Borg, K.A. Vincent, in: W. Kaim, A. Klein (Eds.), Spectroelectrochemistry, RSC Publishing Cambridge, Cambridge, 2008.
[60] The Southampton Electrochemistry Group, Instrumental Methods in Electrochemistry, Horwood Publishing, Lim. Westergate, Chichester, U.K., 2001.
[61] J. Maurer, M. Linseis, B. Sarkar, B. Schwederski, M. Niemeyer, W. Kaim, S. Záliš, C. Anson, M. Zabel, R.F. Winter, J. Am. Chem. Soc. 130 (2008) 259.
[62] S. Záliš, J. Maurer, M. Linseis, R.F. Winter, unpublished results.
[63] F. Hartl, D.J. Stufkens, A. Vlček Jr., Inorg. Chem. 31 (1992) 1687.
[64] F. Paul, B.G. Ellis, M.I. Bruce, L. Toupet, T. Roisnel, K. Costuas, J.-F. Halet, C. Lapinte, Organometallics 25 (2006) 649.
[65] A. Klein, O. Lavastre, J. Fiedler, Organometallics 25 (2006) 635.
[66] N. Gauthier, N. Tchouar, F. Justaud, G. Argouarch, M.P. Cifuentes, L. Toupet, D. Touchard, J.-F. Halet, S. Rigaut, M.G. Humphrey, K. Costuas, P. Paul, Organometallics 28 (2009) 2253.
[67] P. Paul, B.G. Ellis, M.I. Bruce, L. Toupet, T. Roisnel, K. Costuas, J.-F. Halet, K. Lapinte, Organometallics 25 (2006) 649.
[68] S. Sakaki, N. Hagiwara, A. Ohyoshi, J. Phys. Chem. 82 (1978) 1917.
[69] J.B. Raynor, B.G. Jeliazkowa, J. Chem. Soc., Dalton Trans. (1982) 1185.
[70] L.R. Dinelli, A.A. Batista, K. Wohnrath, M.P. de Araujo, S.L. QWueiroz, M.R. Bonfadini, G. Olivia, O.R. Nascimento, P.W. Cyr, K.S. MacFarlane, B.R. James, Inorg. Chem. 38 (1999) 5341.
[71] J. Maurer, P. Mücke, B. Sarkar, W. Kaim, S. Záliš, R.F. Winter, manuscript in preparation.
[72] R.F. Winter, S. Záliš, Coord. Chem. Rev. 248 (2004) 1565.
[73] J. Maurer, R.F. Winter, B. Sarkar, S. Záliš, J. Solid State Electrochem. 9 (2005) 738.
[74] J. Maurer, R.F. Winter, B. Sarkar, J. Fiedler, S. Záliš, Chem. Commun. (2004) 1900.
[75] J. Maurer, B. Sarkar, B. Schwederski, W. Kaim, R.F. Winter, S. Záliš, Organometallics 25 (2006) 3701.
[76] S.K. Seetharaman, M.C. Chung, U. Englich, K. Ruhlandt-Senge, M.B. Sponsler, Inorg. Chem. 46 (2007) 561.
[77] M. Sodupe, J. Bertran, L. Rodriguez-Santiago, E.J. Baerends, J. Phys. Chem. A 103 (1999) 166.
[78] B.J. Lynch, P.L. Fast, M. Harris, D.G. Truhlar, J. Phys. Chem. A 104 (2000) 4811.
[79] M.A. Fox, R.L. Roberts, T.E. Baines, B. Le Guennic, J.-F. Halet, F. Hartl, D.S. Yufit, D. Albesa-Jove, J.A.K. Howard, P.J. Low, J. Am. Chem. Soc. 130 (2008) 3566.
[80] S. Karabunarliev, M. Baumgarten, N. Tyutyulkov, K. Mullen, J. Phys. Chem. 98 (1994) 11892.
[81] C.G. Atwood, W.E. Geiger, J. Am. Chem. Soc. 122 (2000) 5477.
[82] C.G. Atwood, W.E. Geiger, A.L. Rheingold, J. Am. Chem. Soc. 115 (1993) 5310.
[83] T. Ito, T. Hamaguchi, H. Nagino, T. Yamaguchi, H. Kido, I.S. Zavarine, T. Richmond, J. Washington, C.P. Kubiak, J. Am. Chem. Soc. 121 (1999) 4625.
[84] A.B.P. Lever, in: J.A. McCleverty, T.J. Meyer (Eds.), Comprehensive Coordination Chemistry II, Elsevier Science, Amsterdam, 2003, p. 435.
[85] C. Lambert, G. Nöll, J. Am. Chem. Soc. 121 (1999) 8434.
[86] S.F. Nelsen, Chem. Eur. J. 6 (2000) 581.
[87] F. Pevny, R.F. Winter, B. Sarkar, W. Kaim, S. Záliš, Dalton Trans., submitted.
[88] J. Maurer, B. Sarkar, W. Kaim, R.F. Winter, S. Záliš, Chem. Eur. J. 13 (2007) 10257.
[89] M. Linseis, R.F. Winter, B. Sarkar, W. Kaim, S. Záliš, Organometallics 27 (2008) 3321.
[90] A. Hilger, J.-P. Gisselbrecht, R.R. Tykwinski, C. Boudon, M. Schreiber, R.E. Martin, H.P. Lüthi, M. Gross, F. Diederich, J. Am. Chem. Soc. 119 (1997) 2069.
[91] R. Rathore, S.V. Lindeman, A.S. Kumar, J.K. Kochi, J. Am. Chem. Soc. 120 (1998) 6931.
[92] M.G. Giuffreda, M. Bruschi, H.P. Lüthi, Chem. Eur. J. 10 (2004) 5671.
[93] E.L. Spitler, S.P. McClintock, M.M. Haley, J. Org. Chem. 72 (2007) 86.
[94] H. Bock, C. Näther, Z. Havlas, J. Chem. Soc., Chem. Commun. (1995) 1111.
[95] S. Hünig, M. Kemmer, H. Wenner, F. Barbosa, G. Gscheidt, I.F. Perepichka, P. Bäuerle, A. Emge, K. Peters, Chem. Eur. J. 6 (2000) 2618.
[96] G.C. Solomon, D.Q. Andrews, R.H. Goldsmith, T. Hansen, M.R. Wasielewski, R.P. Van Duyne, M.A. Ratner, Am. Chem. Soc. 130 (2008) 17301.
[97] S. Záliš, B. Sarkar, C. Duboc, W. Kaim, Monatsh. Chem. 140 (2009) 765.
[98] E. Waldhör, W. Kaim, M. Lawson, J. Jordanov, Inorg. Chem. 36 (1997) 3248.
[99] R. Gross, W. Kaim, Inorg. Chem. 25 (1986) 4865.
[100] H. Krentzien, H. Taube, Inorg. Chem. 21 (1982) 4001.
[101] M. Moscherosch, E. Waldhör, H. Binder, W. Kaim, J. Fiedler, Inorg. Chem. 34 (1995) 4326.